Received: 25 August 2022 | Revised: 15 May 2023 | Accepted: 12 June 2023

DOI: 10.1002/nbm.4998

RESEARCH ARTICLE

NMR IN BIOMEDICINE WILEY

Fast in vivo assay of creatine kinase activity in the human brain by ^{31}P magnetic resonance fingerprinting

Mark Widmaier [1,2,3] | Song-I Lim [1,2,3] | Daniel Wenz [1,3] | Lijing Xin [1,3]

[1]CIBM Center for Biomedical Imaging, Lausanne, Switzerland

[2]Laboratory for Functional and Metabolic Imaging, École polytechnique fédérale de Lausanne, Lausanne, Switzerland

[3]Animal Imaging and Technology, École polytechnique fédérale de Lausanne, Lausanne, Switzerland

Correspondence
Lijing Xin, CIBM Center for Biomedical Imaging, 1015 Lausanne, Switzerland.
Email: lijing.xin@epfl.ch

Funding information
320030_189064; Swiss National Science Foundation

Abstract

A new and efficient magnetisation transfer ^{31}P magnetic resonance fingerprinting (MT-^{31}P-MRF) approach is introduced to measure the creatine kinase metabolic rate k_{CK} between phosphocreatine (PCr) and adenosine triphosphate (ATP) in human brain. The MRF framework is extended to overcome challenges in conventional ^{31}P measurement methods in the human brain, enabling reduced acquisition time and specific absorption rate (SAR). To address the challenge of creating and matching large multiparametric dictionaries in an MRF scheme, a nested iteration interpolation method (NIIM) is introduced. As the number of parameters to estimate increases, the size of the dictionary grows exponentially. NIIM can reduce the computational load by breaking dictionary matching into subsolutions of linear computational order. MT-^{31}P-MRF combined with NIIM provides T_1^{PCr}, T_1^{ATP} and k_{CK} estimates in good agreement with those obtained by the exchange kinetics by band inversion transfer (EBIT) method and literature values. Furthermore, the test–retest reproducibility results showed that MT-^{31}P-MRF achieves a similar or better coefficient of variation (<12%) for T_1^{ATP} and k_{CK} measurements in 4 min 15 s, than EBIT with 17 min 4 s scan time, enabling a fourfold reduction in scan time. We conclude that MT-^{31}P-MRF in combination with NIIM is a fast, accurate, and reproducible approach for in vivo k_{CK} assays in the human brain, which enables the potential to investigate energy metabolism in a clinical setting.

KEYWORDS
^{31}P MRS, brain energy metabolism, creatine kinase, MRF

Abbreviations: AI, asymmetric inversion; ATP, adenosine triphosphate; BA, Bland–Altman; BMC, Bloch–McConnell; bSSFP, balanced steady-state free precession; BW, bandwidth; CK, creatine kinase; CV, coefficient of variation; EBIT, exchange kinetics by band inversion transfer; FA, flip angle; FAST, four-angle saturation transfer; FID, free induction decay; GI, global inversion; IT, iteration; LR, linear regression; MC, Monte Carlo; ME, matching error; MAPE, mean absolute percentage error; MRF, magnetic resonance fingerprinting; MRS, magnetic resonance spectroscopy; MT, magnetisation transfer; MT-^{31}P-MRF, magnetisation transfer ^{31}P magnetic resonance fingerprinting; NIIM, nested iteration interpolation method; PCr, phosphocreatine; pSNR, peak signal-to-noise ratio; RF, radio frequency; RMSE, root-mean-square error; SAR, specific absorption rate; SLR, Shinar–le Roux; SNR, signal-to-noise ratio; ST, saturation transfer; STD, standard deviation; TR, repetition time; TRiST, triple repetition time saturation transfer; TwiST, two-repetition time saturation transfer.

Mark Widmaier and Song-I Lim contributed equally to this work.

1 | INTRODUCTION

Energy buffering and transport via the phosphocreatine (PCr)/creatine kinase (CK) shuttle play an important role in cellular energy metabolism to maintain cellular adenosine triphosphate (ATP) levels and support neuronal activity and normal brain function.[1] Quantifying the CK activity has been of great interest in the last decades. Chen et al. measured an increase in the CK rate during visual stimulation, indicating that the CK turnover is elevated (34%) upon increased neuronal activity.[2] In another study, a decline of the CK rate (26%) with age has been found in rats using an in vivo ^{31}P saturation transfer (ST) experiment.[3] Alteration of the CK rate (14–22%) could result in abnormal cellular function and has also been reported in several psychiatric and metabolic disorders.[4–6] These noninvasive measurements of CK reaction rates have been achieved using ^{31}P magnetic resonance spectroscopy (MRS) combined with magnetisation transfer (MT). However, MT methods typically require a long acquisition time due to the low metabolite concentrations, low signal-to-noise ratio (SNR), and long T_1 relaxation times, which limits their clinical applications.

In an effort to shorten the scan time, several fast ^{31}P MT-MRS methods have been introduced based on the ST technique.[7,8] Four-angle saturation transfer (FAST)[9] and triple repetition time saturation transfer (TRiST)[10] are performed under partially saturated conditions with a reduced repetition time (TR) and reduced number of required spectra. The accuracy of FAST depends on the accuracy of the excitation flip angles (FAs) used for the dual-angle-based T_1 measurement. Further, the number of acquired spectra can be reduced by using empirical T_1 values, such as the two-repetition time saturation transfer (TwiST)[11] and nominal T_1[12] methods.

However, the ST technique, which uses a long RF pulse train for magnetisation saturation, can induce undesirable high specific absorption rate (SAR) (especially limiting human brain applications), off-resonance saturation effects, and the activation of small hidden pools.[13–15] As an alternative, inversion transfer methods, such as exchange kinetics by band inversion transfer (EBIT)[16] and others,[17–26] have been introduced, by which the MT effect in a selected pathway can be amplified through band inversion of the spins that are involved in competitive pathways.

^{31}P magnetic resonance fingerprinting (MRF) has shown its feasibility and robustness in CK flux measurement in rat skeletal muscle using balanced steady-state free precession (bSSFP)-type sequences with a series of varying FAs following an ST pulse train.[27] The introduced method, ^{31}P CK-MRF, showed lower coefficient of variation (CV) values within a sevenfold shorter acquisition duration than the FAST technique. However, in order to reduce the computational complexity, several parameters were fixed instead of being estimated together with k_{CK}. Furthermore, ST is difficult to apply in clinical studies due to the intensive RF power deposition. Therefore, the ^{31}P MRF technique needs to be adapted for clinical applications with a reduced SAR and a novel matching approach for multiparametric estimation.

The purpose of the study is to demonstrate the feasibility of the MT-^{31}P-MRF approach at 7T in the human brain, to evaluate its robustness, and to compare its test–retest reproducibility with EBIT. First, MT-^{31}P-MRF is designed based on selective inversion transfer to reduce SAR in the human brain. To address the challenge of creating and matching large multiparametric dictionaries in an MRF scheme, a nested iteration interpolation method (NIIM) is introduced, which combines efficient iterative parameter estimation with small dictionaries and an interpolation approach to provide a bias-free estimation. Second, the acquisition and parameter estimation method are validated using simulations and in vivo measurements. The accuracy of parameter estimation is evaluated by simulations. Last, test–retest reproducibility analyses are performed by scanning the same volunteer twice using both MT-^{31}P-MRF and EBIT methods.

2 | METHODS

2.1 | Pulse sequence

The MT-^{31}P-MRF approach is based on a bSSFP-type sequence. The transient state is reached by variable FAs with a phase alternation of 180°. 1D localisation is achieved by a 1.5-ms Shinar–le Roux (SLR) pulse (bandwidth (BW) of 6.6 kHz). The repetition time is set to $T_R = 18.9$ ms with a sampling rate of 256 points per 16.67 ms acquisition time, resulting in a 60 Hz spectral resolution and 15.36 kHz spectral BW. The sequence scheme consists of three parts. Part I (Figure 1A) consists of two HS4 global inversion (GI) pulses with 10.35 ms duration with a BW of 4.9 kHz, to invert all ^{31}P metabolites of interest in the spectral range from −20.3 to 20.3 ppm. Both GIs increase the sensitivity of the MRF signals for T_1 relaxation. The two GI pulses are followed by 249 and 269 RF pulses in a sinusoidal pattern, respectively.[28] Part II (Figure 1A) consists of 180 RF pulses with abruptly changing FA patterns to detect B_1 inhomogeneities and off-resonance via the PCr signal.[29] The acquisition time of Part I and II is 18.5 s combined, including a 5 s relaxation delay between repetitions. In Part III (Figure 1B), selective inversion by two asymmetric inversion pulses (AI1 and AI2)[30] is applied to increase the sequence sensitivity for k_{CK}.[16] The two AIs have opposite inversion profiles, with the carrier frequency set to −1.25 ppm. AI1 is used to invert P_i and PCr, and AI2 is used to invert α, β, and γ-ATP. AI1 and AI2 are followed by a train of 185 and 59 RF pulses, respectively. Part III takes 9 s, including a 4 s relaxation delay between repetitions. Each measurement has one dummy scan to reach the steady state. The overall number of FAs combining all three parts (I, II, III) is $L = 943$.

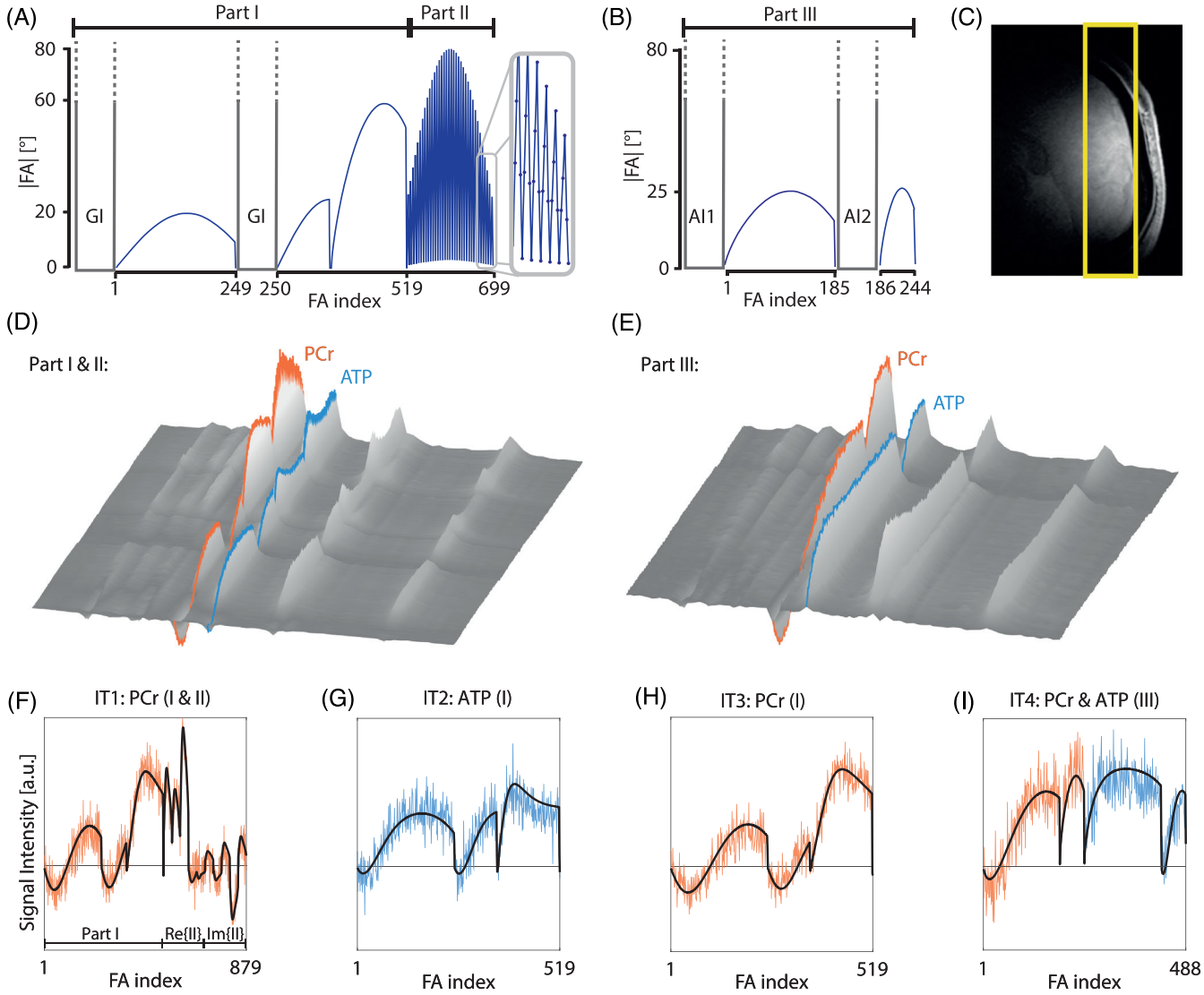

FIGURE 1 Sequence diagram with FA patterns of (A) Parts I and II and (B) Part III. (C) An exemplary 20 mm selected slice in the occipital lobe. Resulting grouped average waterfall spectra of (D) Parts I and II and (E) Part III over the FA index. (F–I) Example of the NIIM matching procedure for $k_{CK}^{0,2} = 0.3\,s^{-1}$ from single subject data (full length acquisition). Black lines indicate the matched dictionary entries. In vivo signal evolution of PCr is marked in orange, and that of γ-ATP is marked in blue. The part used is indicated in the title.

2.2 | Fingerprint simulation

A dictionary is created for each subject using the Bloch–McConnell (BMC) equations. PCr and γ-ATP are represented in a two-pool exchange model with the two pools a and b.[27] The PCr pool, a, is resonating at

$$f_0^a = f_0^{PCr} + f_{off} + f_{dist,i}, \tag{1}$$

where f_0^{PCr} is the resonance frequency of PCr, $f_{dist,i}$ is the off-resonance frequency of the i-th isochromat of the underlying subject-specific B_0 distribution, and f_{off} is the shift of the B_0 distribution. γ-ATP (pool b) is a doublet, and the two resonance peaks are incorporated as two subpools, b_1 and b_2, with resonance frequencies of

$$f_0^{b_1} = f_0^{ATP} + f_{off} + f_{dist,i} + 0.5J \tag{2}$$

and

$$f_0^{b_2} = f_0^{ATP} + f_{off} + f_{dist,i} - 0.5J, \tag{3}$$

where f_0^{ATP} is the resonating frequency of γ-ATP and J is the J-coupling constant of 16.1 Hz. No exchange of magnetisation between the two sub-pools is assumed, and the equilibrium magnetisation is split evenly.

To decrease the simulation complexity, the magnetisation equation for an arbitrary discrete time step Δt is described as $\mathbf{M}_L$ for the longitudinal magnetisation and $\mathbf{M}_T$ for the transverse magnetisation, as follows:

$$\mathbf{M}_L^{j+1} = e^{\mathbf{A}_L \Delta t}\mathbf{M}_L^j + \mathbf{R} \tag{4}$$

and

$$\mathbf{M}_T^{j+1} = e^{\mathbf{A}_T \Delta t}\mathbf{M}_T^j, \tag{5}$$

where $\mathbf{M}^j$ and $\mathbf{M}^{j+1}$ are the magnetisations before and after Δt. The magnetisation vectors are

$$\mathbf{M}_L = \left[M_z^a \;\; M_z^{b_1} \;\; M_z^{b_2}\right]^T, \tag{6}$$

$$\mathbf{M}_T = \left[M_x^a \;\; M_y^a \;\; M_x^{b_1} \;\; M_y^{b_1} \;\; M_x^{b_2} \;\; M_y^{b_2}\right]^T. \tag{7}$$

The longitudinal recovery term is defined as

$$\mathbf{R} = (e^{\mathbf{A}_L \Delta t} - \mathbf{I})\mathbf{A}_L^{-1} M_0^a \left[\frac{1}{T_1^a} \;\; \frac{0.5}{C_r T_1^b} \;\; \frac{0.5}{C_r T_1^b}\right]^T, \tag{8}$$

where $\mathbf{I}$ is the identity matrix, $[\bullet]^{-1}$ is the matrix inverse, T_1^a and T_1^b are the longitudinal relaxation times of PCr and γ-ATP, and the concentration ratio is

$$C_r = \frac{M_0^a}{M_0^b}, \tag{9}$$

with equilibrium magnetisations M_0^a and M_0^b of pools a and b, respectively.

The free precession, relaxation, and magnetisation exchange matrices for longitudinal and transverse magnetisation can be described as

$$\mathbf{A}_L = \begin{bmatrix} -\frac{1}{T_1^a} - k_{CK} & k_{CK,r} & k_{CK,r} \\ 0.5k_{CK} & -\frac{1}{T_1^b} - k_{CK,r} & 0 \\ 0.5k_{CK} & 0 & -\frac{1}{T_1^b} - k_{CK,r} \end{bmatrix} \tag{10}$$

and

$$\mathbf{A}_T = \begin{bmatrix} -\frac{1}{T_2^a} - k_{CK} & \omega_a & k_{CK,r} & 0 & k_{CK,r} & 0 \\ -\omega_a & -\frac{1}{T_2^a} - k_{CK} & 0 & k_{CK,r} & 0 & k_{CK,r} \\ 0.5k_{CK} & 0 & -\frac{1}{T_2^b} - k_{CK,r} & \omega_{b_1} & 0 & 0 \\ 0 & 0.5k_{CK} & -\omega_{b_1} & -\frac{1}{T_2^b} - k_{CK,r} & 0 & 0 \\ 0.5k_{CK} & 0 & 0 & 0 & -\frac{1}{T_2^b} - k_{CK,r} & \omega_{b_2} \\ 0 & 0.5k_{CK} & 0 & 0 & -\omega_{b_2} & -\frac{1}{T_2^b} - k_{CK,r} \end{bmatrix}, \tag{11}$$

where the forward creatine kinase rate constant is k_{CK} (a → b) and the reverse rate constant is

$$k_{CK,r} = k_{CK} \cdot C_r. \tag{12}$$

The precession frequencies of pools a and b are $\omega_a = 2\pi f_0^a$ and $\omega_{b_{1,2}} = 2\pi f_0^{b_{1,2}}$ and their transverse relaxation times are T_2^a and T_2^b, respectively.

The slice profile[31] and a linear coil sensitivity approximation of the surface coil are incorporated. The excitation profile is modeled as a sum of N_f subslices. In each subslice, the effective excitation of the -l-th FA, $\phi_{eff}(l,n_f)\,(n_f = 1,\ldots,N_f)$, is defined as

$$\phi_{eff}(l,n_f) = (-1)^{l-1} \cdot C_{SP}(n_f) \cdot C_{CS}(n_f) \cdot C_{B1} \cdot \phi(l), \tag{13}$$

where $\phi(l)$ is the nominal l-th FA of the MRF pattern. The 0° and 180° phase alternation of the RF pulses is indicated for each FA by $(-1)^{l-1}$. Further on, C_{SP} is the excitation pulse profile, C_{CS} is the coil sensitivity profile (taken as the coil sensitivity profile given in Equation 20), and C_{B1} is the scaling factor of B_1,

$$C_{B1} = \frac{B_1}{B_{1,nom}}, \tag{14}$$

where $B_{1,nom}$ is the nominal transmit field strength to reach ϕ and B_1 is the actual transmit magnetic field strength. B_1 and the FAs are assumed to be the same for all pools. FAs are simulated by a spontaneous rotation around the x-axis:

$$\begin{bmatrix} \mathbf{M}_T^+(l,n_f) \\ \mathbf{M}_L^+(l,n_f) \end{bmatrix} = \mathbf{R}_x(l,n_f) \begin{bmatrix} \mathbf{M}_T^-(l,n_f) \\ \mathbf{M}_L^-(l,n_f) \end{bmatrix}, \tag{15}$$

where $\mathbf{M}_T^-$ and $\mathbf{M}_L^-$ are the transversal and longitudinal magnetisations before the excitation pulse and $\mathbf{M}_T^+$ and $\mathbf{M}_L^+$ are those after the excitation pulse. The rotation matrix, $\mathbf{R}_x$, is described as

$$\mathbf{R}_x(l,n_f) = \begin{bmatrix} 1 & 0 & 0 & 0 & 0 & 0 & 0 & 0 & 0 \\ 0 & \cos(\phi_{eff}(l,n_f)) & 0 & 0 & 0 & 0 & -\sin(\phi_{eff}(l,n_f)) & 0 & 0 \\ 0 & 0 & 1 & 0 & 0 & 0 & 0 & 0 & 0 \\ 0 & 0 & 0 & \cos(\phi_{eff}(l,n_f)) & 0 & 0 & 0 & -\sin(\phi_{eff}(l,n_f)) & 0 \\ 0 & 0 & 0 & 0 & 1 & 0 & 0 & 0 & 0 \\ 0 & 0 & 0 & 0 & 0 & \cos(\phi_{eff}(l,n_f)) & 0 & 0 & -\sin(\phi_{eff}(l,n_f)) \\ 0 & \sin(\phi_{eff}(l,n_f)) & 0 & 0 & 0 & 0 & \cos(\phi_{eff}(l,n_f)) & 0 & 0 \\ 0 & 0 & 0 & \sin(\phi_{eff}(l,n_f)) & 0 & 0 & 0 & \cos(\phi_{eff}(l,n_f)) & 0 \\ 0 & 0 & 0 & 0 & 0 & \sin(\phi_{eff}(l,n_f)) & 0 & 0 & \cos(\phi_{eff}(l,n_f)) \end{bmatrix}. \tag{16}$$

In each subslice, the signal evolution is modeled by a weighted sum of isochromats. The weight w_i and off-resonance $f_{dist,i}$ of each isochromat's signal evolution are determined by the subject-specific B_0 distribution. The B_0 distribution is found using the histogram of the measured B_0 map with a 1 Hz resolution. Compared with the original imaging MRF approach,[28] spectral leakage due to fast Fourier transformation is an additional weighting factor. We modeled this effect by simulating each point of the free induction decay (FID) during each T_R. Overall, the l-th spectrum S_l is therefore

$$S_l = \mathcal{F}\left\{ \sum_{n_f=1}^{N_f} \sum_i w_i s_l^{n_f,i} \right\}, \tag{17}$$

where $s_l^{n_f,i}$ is the l-th time domain FID signal in the n_f-th subslice of the i-th isochromat and $\mathcal{F}\{\bullet\}$ is the Fourier transformation operator. Finally, the signal evolutions (fingerprints) of PCr and γ-ATP stored in the dictionary are extracted from the peak intensity of each metabolite over the L spectra (same as in vivo signal evolution extraction: Figure 1D,E).

2.3 | Dictionary generation and parameter matching

For all dictionaries, T_2^{PCr}, T_2^{ATP}, and the resonance frequencies f_0^{PCr} and f_0^{ATP} are set according to literature values[32] to 135 ms, 30 ms, 0 ppm, and −2.52 ppm, respectively. The remaining six parameters, C_{B1}, f_{off}, T_1^{PCr}, T_1^{ATP}, C_r, and k_{CK}, are objectives of the estimation. Matching proceeds with

the inner product of the L_2 norm of the measured pattern and the dictionary entries.[28] To estimate such a high-dimensional parameter set, we introduce NIIM. NIIM combines an iterative and interpolating approach to drastically reduce dictionary creation and matching time (Figure 2). The problem is solved by repeating N times an iterative estimation loop followed by a final interpolation step. In this study, $N = 5$ iterative estimation loops are used. Each iterative loop has a varying initial condition of the creatine kinase rate $k_{CK}^{0,n}$ ($k_{CK}^{0} = 0.2, 0.3, 0.35, 0.4, 0.5$), with $n = 1,\ldots,N$ and fixed initial values of $T_1^{0,ATP}$, $T_1^{0,PCr}$, and C_r^0. Each iterative loop encloses four iterative steps (IT1 to IT4) described in 2.3.4 Iterative part. In each successive iterative step, a dictionary is created to estimate the respective free parameter(s). With the advance in iterative steps, the dictionary is created using fewer initial values, while more estimated values from the prior iterative step(s) are used. In the last iterative step (IT4), k_{CK}^n is estimated. The resulting estimates in each loop (f_{off}^n, C_{B1}^n, $T_1^{n,ATP}$, $T_1^{n,PCr}$, C_r^n, k_{CK}^n) are biased depending on the $k_{CK}^{0,n}$. The association between the N biased estimates $k_{CK}^1,\ldots,k_{CK}^N$ and their respective k_{CK}^0 is exploited to find a corrected final estimate, k_{CK} (described in 2.3.2 Interpolation part). This correction, using a linear regression function, proceeds in the final interpolation step. Afterwards, the final k_{CK} is used to correct the other free parameters. All matchings and dictionary creations were performed on an Intel Xeon Silver 4216.

2.3.1 | Iterative part

In IT1, C_{B1}^n and f_{off}^n are determined by matching the concatenated signal evolution of PCr (Parts I and II, Figure 1F). For each $k_{CK}^{0,n}$, a dictionary is created with 76 values of C_{B1} (from 0.60 to 1.35) and 21 values of f_{off} (from −10 Hz to 10 Hz). Initial values of $T_1^{0,PCr}$, $T_1^{0,ATP}$, and C_r^0 are assumed to be 5 s, 1 s and 1.33, respectively.

In the second (IT2) and third (IT3) iteration steps, the longitudinal relaxation times $T_1^{n,ATP}$ and $T_1^{n,PCr}$ are estimated. The estimated $\hat{f}_{off}^n$ and C_{B1}^n from IT1 and initial values for $T_1^{0,PCr}$ and C_r^0 are used in IT2 to create a dictionary for γ-ATP to estimate $\hat{T}_1^{n,ATP}$. Afterwards, in IT3, a dictionary to estimate T_1^{PCr} is created using the prior estimates (f_{off}^n, C_{B1}^n, and $T_1^{n,ATP}$). $T_1^{n,ATP}$ and $T_1^{n,PCr}$ are matched using Part I of the γ-ATP and PCr signals, respectively (Figure 1G,H). T_1 values are varied with 31 steps and a 2.5% incremental step from the lower bound value $T_{1,lb}^{n,PCr}$ and $T_{1,lb}^{n,ATP}$ depending on $k_{CK}^{0,n}$ ($T_{1,lb}^{PCr} = 3.00, 3.25, 3.50, 3.75, 4.00$ s; $T_{1,lb}^{ATP} = 0.65, 0.62, 0.60, 0.58, 0.55$ s). The concentration ratio C_r^n is determined after IT2 and IT3 as

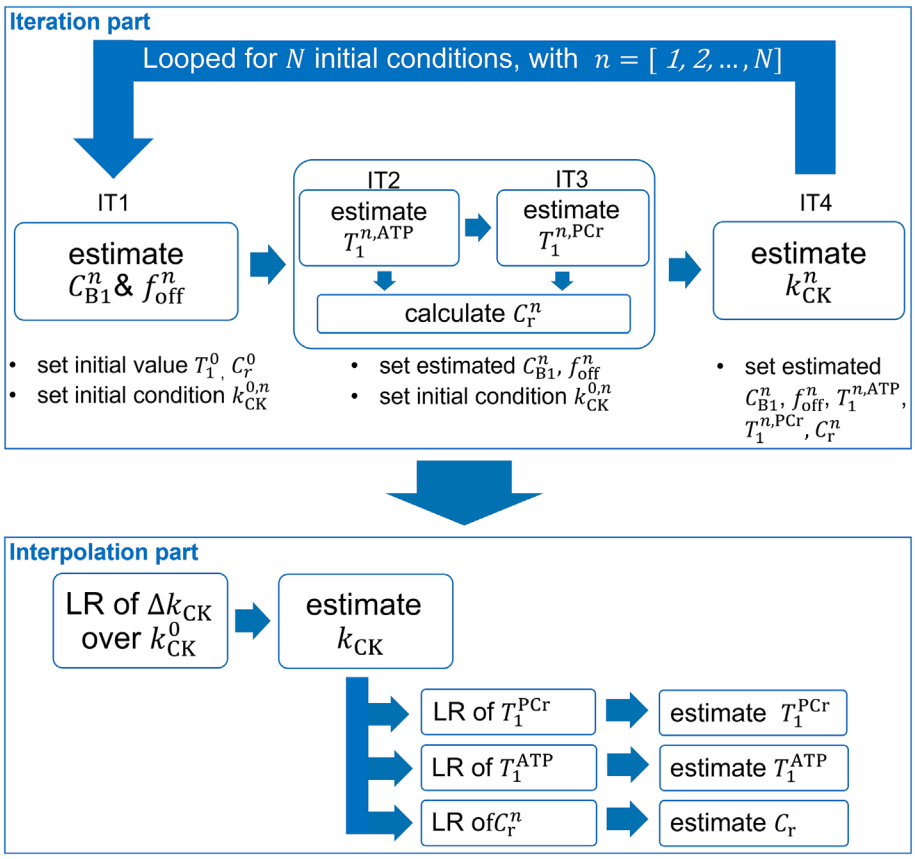

FIGURE 2 The NIIM schematic used for the in vivo data parameter estimation.

$$C_r^n = \frac{1}{L_{PI}} \sum_{l=1}^{L_{PI}} \frac{S_{l,sim}^{n,ATP} \cdot S_{l,mes}^{PCr}}{S_{l,mes}^{ATP} \cdot S_{l,sim}^{n,PCr}}, \tag{18}$$

where L_{PI} is the number of FAs in Part I, and l is the FA index with its respective measured signal of PCr $S_{l,mes}^{PCr}$ and γ-ATP $S_{l,mes}^{ATP}$, matched simulated PCr signal $S_{l,sim}^{n,PCr}$, and matched simulated γ-ATP signal $S_{l,sim}^{n,ATP}$ of the n-th iterative loop.

In IT4, the remaining free parameter k_{CK}^n is determined. The last set of dictionaries is simulated for Part III using the five previously estimated parameters. The dictionary contains 61 steps of k_{CK} ranging from $0.10\,s^{-1}$ to $0.70\,s^{-1}$ with an incremental step of $0.01\,s^{-1}$. The matching is proceeded with the concatenated Part III of the γ-ATP and PCr signal evolution (Figure 1I).

2.3.2 | Interpolation part

Each k_{CK}^n may be a biased estimate dependent on the difference between the underlying k_{CK} and $k_{CK}^{0,n}$. As demonstrated by simulations (Figure 3), the dependence can be assumed to be linear. The final estimate, k_{CK}, is found by determine the zero-crossing of the linear regression (LR). The LR is determined using N datapoints over k_{CK}^0 in a least-squares sense (example in Figure 3A). Each datapoint is calculated by the difference

$$\Delta k_{CK}^n = k_{CK}^n - k_{CK}^{0,n}. \tag{19}$$

Furthermore, simulations showed that the other free parameters are linearly dependent on $k_{CK}^{0,n}$ (described in the next section). Therefore, LR values for each free parameter from the N estimates over $k_{CK}^{0,n}$ are computed. The bias-corrected estimate of each parameter is then found by determining the linear regression function value at $k_{CK}^0 = k_{CK}$. Figure 3B,C illustrates this process for T_1^{PCr} and T_1^{ATP}, respectively.

2.4 | Error estimation by simulations

To investigate the impact of a biased initial condition of k_{CK}^0 on the estimation of k_{CK}, T_1^{ATP} and T_1^{PCr}, simulations are performed with underlying ground-truth values set to $k_{CK} = 0.37\,s^{-1}$, $T_1^{PCr} = 5.0\,s$, $T_2^{PCr} = 135\,ms$, $T_1^{ATP} = 1.0\,s$, $T_2^{ATP} = 30\,ms$, $C_r = 1.33$, $C_{B1} = 1$, and $f_{off} = 0\,Hz$. The created signal evolutions of PCr and γ-ATP are then processed by five iterative loops, with the same initial values as described in the iterative part. A linear dependence is found between $k_{CK}^{0,n}$ and the estimated free parameters. This property is exploited in the interpolation part of the NIIM.

To estimate the matching error (ME) introduced by the NIIM approach, noiseless signal evolutions are simulated and processed by the full estimation procedure with the $N = 5$ initial conditions of k_{CK}^0. The underlying ground-truth values are altered for one parameter at a time. The other parameters are set to their center value. The center value of the parameters are $k_{CK} = 0.35\,s^{-1}$, $C_{B1} = 1$, $f_{off} = 0\,Hz$, the initial values ($T_1^{PCr} = 5\,s$, $T_1^{ATP} = 1\,s$, $C_r = 1.33$) or fixed values ($T_2^{PCr} = 135\,ms$, $T_2^{ATP} = 30\,ms$). The ground-truth value of the altered parameter is varied in a range

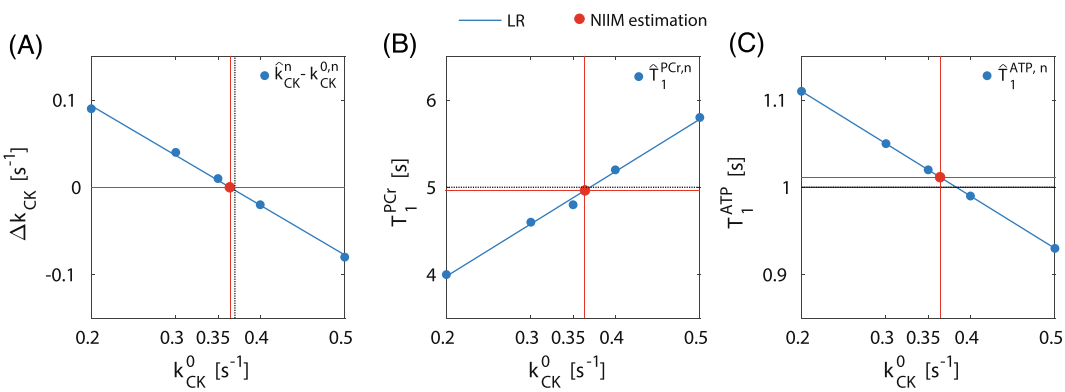

FIGURE 3 (A) Δk_{CK}^n, (B) $T_1^{PCr,n}$, and (C) $T_1^{ATP,n}$ over k_{CK}^0 and their LR. The ground-truth values of k_{CK}, T_1^{PCr}, and T_1^{ATP} are marked by a dotted line. The NIIM estimation of $\Delta k_{CK} = 0\,s^{-1}$ and the other parameter estimates are marked by red dots.

of $\pm 50\%$ from the center value with a 5% step (except f_{off}: ± 20 Hz, 1Hz step). The dictionaries are generated with 50 steps and a step size of 2.5% of their center values (f_{off} dictionary range in IT1: 1Hz step from -25 Hz to 25 Hz).

Finally, the noise robustness of the NIIM is evaluated by Monte Carlo (MC) simulations. For each signal evolution, the ground-truth values of k_{CK}, T_1^{ATP}, T_1^{PCr}, and C_r are randomly assigned in ranges from 0.2 s^{-1} to 0.5 s^{-1}, 0.7 s to 1.3 s, 4 s to 7 s, and 1 to 1.67 respectively. C_{B1} and f_{off} are assigned randomly following a Gaussian distribution ($C_{B1} \sim \mathcal{N}(1, 0.05^2)$ and $f_{off} \sim \mathcal{N}(0, 3^2)$ [Hz]). Gaussian noise with different power levels is added to each signal evolution to create data with SNR values of 0, 3, 6, 9, 12, and 30 dB. 1000 signal evolutions of PCr and γ-ATP are simulated for each SNR level and in total 6000 signal evolutions are processed with NIIM.

2.5 | In vivo experimental protocol

In vivo experiments were performed to show the feasibility of MT-^{31}P-MRF and to compare the obtained values and reproducibility with EBIT. The data were acquired from six healthy subjects (three females and three males; age 18 to 30 years) who provided written informed consent. All MR experiments were performed with a 7T/68 cm MR scanner (Siemens Medical Solutions, Erlangen, Germany) with ^{1}H quadrature surface coils (10 cm diameter) and a single-loop ^{31}P coil (7 cm diameter) on the occipital lobe. A 20 mm slice parallel to the coil's transversal plane was examined (Figure 1C).

B_0 shimming is performed using a 3D map, shim and PCr line-width measurements are performed each time to control the spectral quality for fair comparison between the two methods. The EBIT[16] sequence consisted of an asymmetric adiabatic inversion pulse[30] applied at -1.25 ppm (Module I: inversion of ATPs) and 1.25 ppm (Module II: inversion of PCr and ATPs), followed by multiple inversion delays T_d and a SLR excitation pulse ($T_R = 4$ s; $T_d = 60$, 200, 400, 670, 1590, 3000 ms; 16 averages per T_d; one dummy scan; 6000 Hz spectral bandwidth; 20 mm slice thickness). Reference scans are acquired using the same sequence without the inversion pulse ($T_R = 4$ and 20 s; 16 and 6 signal averages; one dummy scan). Modules I and II target PCr $\rightarrow \gamma$-ATP and $P_i \rightarrow \gamma$-ATP, respectively. The total scan duration of EBIT with reference scans is 17 min 4 s.

The MT-^{31}P-MRF sequence is used to estimate the relaxation parameters and the forward creatine kinase rate constant k_{CK} (PCr $\rightarrow \gamma$-ATP) in the same 20mm slice as EBIT. The sequence is performed as described above, with the transmit/receive frequency centred at the resonance frequency of PCr. 37 measurements of Parts I and II and one dummy scan are applied, followed by the same number of measurements and dummy scans of Part III. A proton B_0 map (6 s) is acquired afterwards to measure the off-resonance distribution in the slice. The total scan time is 17 min 24 s. NIIM used $N = 5$ initial conditions ($k_{CK}^0 = 0.20$, 0.30, 0.35, 0.40, 0.50 s^{-1}). Furthermore, the subslice number N_f was set to 19 and the coil sensitivity profile was set to

$$C_{CS}(n_f) = 1.8 - \frac{1.6(n_f - 1)}{N_f - 1}, \tag{20}$$

according to a linear approximation of the B_1 profile of a surface coil with radius of 3.5 cm.[33]

To evaluate test–retest reproducibility, each volunteer was scanned twice using the EBIT and MRF protocol with a 10-min break between sessions. The order of EBIT and MRF applications is randomised to avoid systematic error.

2.6 | ^{31}P MRS EBIT and MT-^{31}P-MRF in vivo data processing

All data processing was performed using MATLAB (MathWorks, Natick, MA, USA). For the EBIT data, 6 Hz of line broadening is applied to the free induction decay before Fourier transformation. A Voigt line shape is used for fitting each ^{31}P MR peak. The fully relaxed ^{31}P spectra ($T_R = 20$ s; with apparent $T_{1,ap}^{PCr} = 3.8$ s[32]) were used to calculate the equilibrium PCr/γ-ATP magnetisation ratio. Normalised longitudinal magnetisation is acquired using the reference scan ($T_R = 4$ s). The intensities of peaks acquired from Modules I and II are concatenated. Fitting of the two-pool exchange model (Supplementary Material S1) is performed using the least-squares function *lsqcurvefit*.[16]

The MT-^{31}P-MRF data of an individual subject, containing the spectra for all FAs and averages, is a $256 \times n_{avg} \times L$ complex tensor. The signal evolutions of PCr and γ-ATP are extracted from signal intensities (complex data) at 0 and -2.49 ppm respectively, resulting in a $2 \times n_{avg} \times L$ tensor. Before averaging along the second dimension, the complete signal evolution is phased by the mean zero-order phase calculated in Part I. The final signal evolutions are processed further in the NIIM matching procedure as described above.

To evaluate the effect of SNR on parameter estimations, both EBIT and MT-^{31}P-MRF data are split into subsets with different numbers of averages to reach different in vivo SNR conditions. Out of the complete set of 37 MRF averages per subject, subsets were generated (consecutive measurements), with n_{avg} =37, 27, 19, 11, 8 and 4 averages to mimic scan times of 17 min 24 s, 12 min 50 s, 9 min 17 s, 5 min 30 s, 4 min 15 s and 2 min 18 s, respectively. The EBIT data were split in subsets with 16, 12, 8 and 4 averages to mimic scan times of 17 min 4 s, 13 min, 9 min 15 s and 5 min 30 s, respectively.

2.7 | Statistical analysis and SNR estimation

Statistical analysis was performed using MATLAB. The matching error (ME) is calculated as the relative deviation of an estimated parameter X to its underlying ground truth X_{true}, where

$$\text{ME} = \frac{X - X_{\text{true}}}{X_{\text{true}}} \cdot 100\%. \tag{21}$$

The mean absolute percentage error (MAPE) is used to evaluate the NIIM performance in the MC simulations. MAPE is defined as the mean absolute ME over N_s samples, such that

$$\text{MAPE} = \frac{100\%}{N_s} \sum_{n_s=1}^{N_s} |\text{ME}_{n_s}|. \tag{22}$$

For this MC simulation, MAPE is calculated for each parameter over all $N_s = 1000$ estimates per noise level.

To assess test–retest reproducibility between the two sessions for both methods, the coefficient of variation (CV),

$$\text{CV} = \frac{\sqrt{\text{E}[(X - \text{E}[X])^2]}}{\text{E}[X]}, \tag{23}$$

is used, where $\text{E}[X]$ is the expected value. The CV is always computed between the two measurements and the same indexed group averages. Mean and STD are calculated across all subjects and group averages. Furthermore, the Bland–Altman (BA) comparison is used to compare EBIT with MT-^{31}P-MRF for the repeated measurement[34] and the simulation results.

The SNR is evaluated using the *snr* function of MATLAB. This function estimates the SNR in [dB] as the ratio between the signal power and noise power. The matched dictionary entry and the residual of the matched and the measured signal as noise approximation are used as the inputs of the function. As a second SNR evaluation, we used the traditional peak SNR (pSNR). For the MRF, it is defined as the maximum peak amplitude of the PCr signal in Part I divided by the root-mean-square error (RMSE) calculated from the spectra in ranges of −37.91 to −17.96 ppm and 14.46 to 37.91 ppm. For EBIT, the peak amplitude of the PCr signal in the reference scan ($T_R = 4$ s) was divided by the RMSE in a range between 20 and 30 ppm. Maximum PCr signal intensity was taken to lie between −2 and 2 ppm.

3 | RESULTS

3.1 | Simulation validation

Figure 3 examines the LR on which the interpolation part of the NIIM is based. At the zero-crossing of the LR function, the estimated k_{CK} is equal to $k_{\text{CK}}^0 = 0.364\,\text{s}^{-1}$ (Figure 3A). The estimated k_{CK} is within one quantification step of the k_{CK} dictionary of IT4. Then, T_1^{PCr} and T_1^{ATP} are determined by their LRs over k_{CK}^0 (Figure 3B,C). The full NIIM matching procedure on three noiseless signal evolutions, with random assigned ground-truth values (Table S2.1) is illustrated in the supplementary material S2 (iterative (Figure S2.1) and interpolation part (Figure S2.2)).

Further simulations are performed, to evaluate the impact of biased initial values and/or conditions on the estimation accuracy. Figure 4 shows the simulation results of the ME for different free parameters (C_{B1} and f_{off} are shown in supplementary Figure S3.1). Less than 5% matching errors are mostly expected for all estimated parameters in the investigated range of k_{CK}, T_1^{PCr}, T_1^{ATP}, and C_r. At the boundaries of the investigated range, the ME for T_1^{PCr} and T_1^{ATP} reached 11%. Since T_2 was not included in the estimation process, a bias in the assumed T_2^{ATP} and T_2^{PCr} leads to a different extent of bias in the estimated parameters, especially for k_{CK} values. A bias of −25% to 50% in k_{CK} may be introduced by a ±50% bias in the T_2^{PCr} value. The bias in all assumed parameter values has no impact on the estimation of off-resonance f_{off} (not shown).

The NIIM accuracy is also evaluated with MC simulations, using signal evolutions with different SNRs. The MAPE for k_{CK} is approximately 5% for SNR above 12 dB. Both the MAPE and STD of the absolute percentage error increase with decreasing SNR, as shown in Figure 5A. At 0 dB, the MAPE of k_{CK}, T_1^{ATP}, and T_1^{PCr} does not exceed 10%. The k_{CK} estimates correlate with the ground-truth values at an SNR of 12 dB (Table 1: $\text{SNR}_{\text{PCr}} = 12.0$ dB; $n_{\text{avg}} = 37$) with an R^2 value of 0.98, as shown in Figure 5B. The BA plot in Figure 5C shows the comparison of the NIIM k_{CK} estimates with the ground-truth values, demonstrating only a slight offset in the estimation (0.007 s^{-1} with an 1.96 STD of 0.037 s^{-1}.

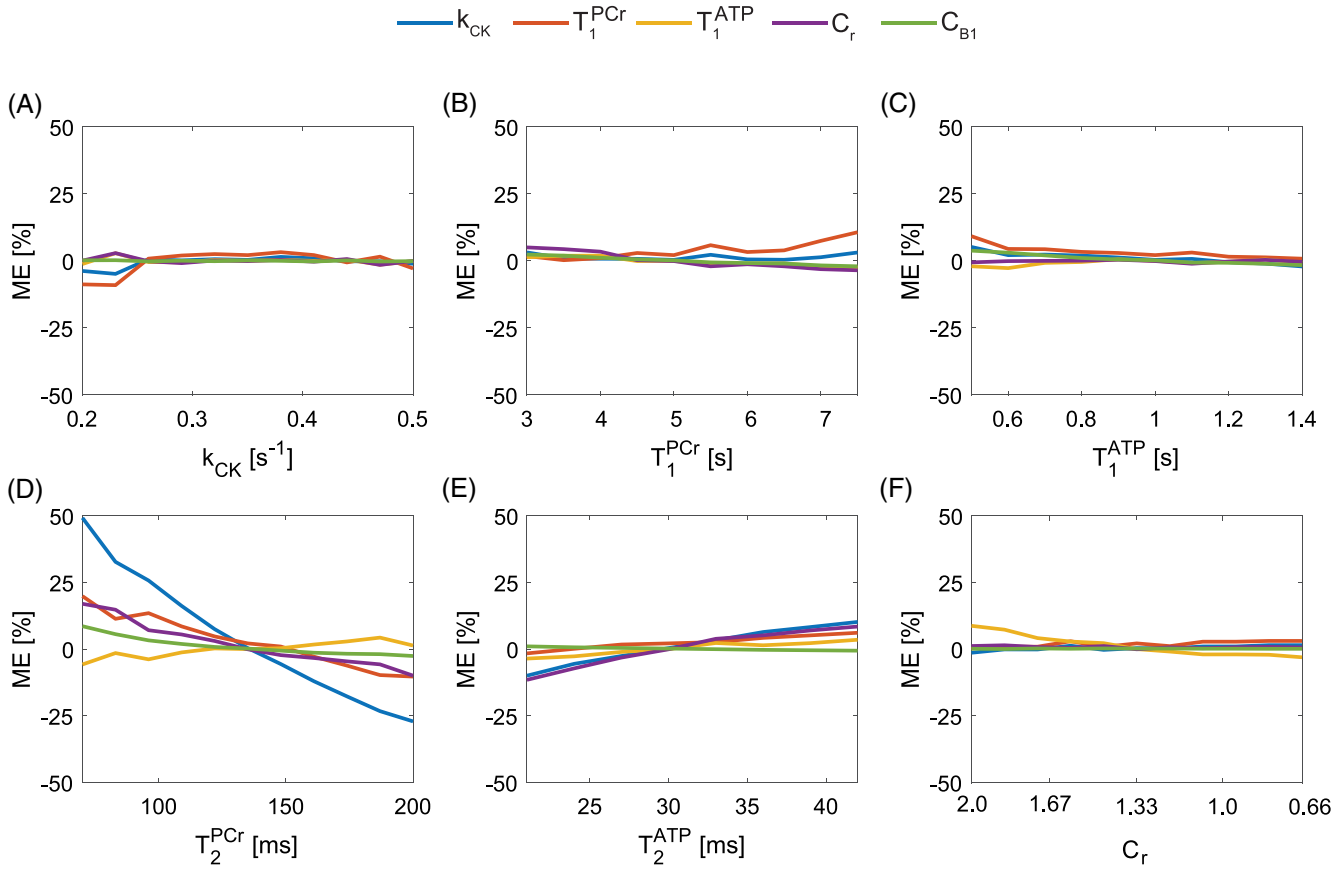

FIGURE 4 The ME of free parameters introduced by the bias in the initial condition (A) k_{CK} or initial values (B) T_1^{PCr}, (C) T_1^{ATP}, (D) T_2^{PCr}, (E) T_2^{ATP}, and (F) C_r. Noiseless signal evolutions with varying underlying ground-truth parameters were simulated and evaluated with NIIM using fixed initial conditions and values.

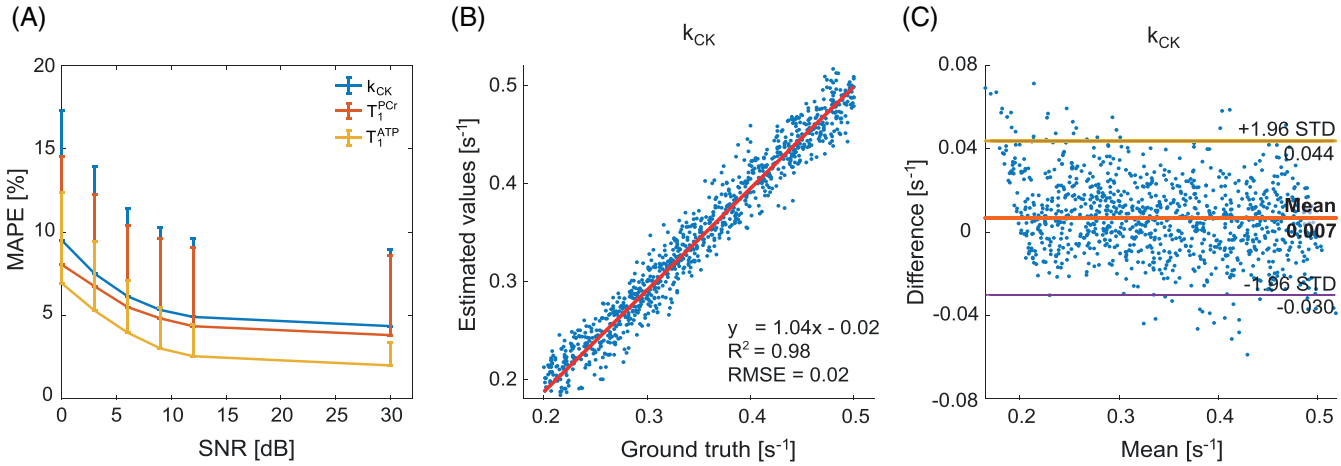

FIGURE 5 (A) Evaluation of the NIIM estimation performance on signal evolutions with randomly assigned ground-truth parameters. The MAPE of k_{CK}, T_1^{PCr}, and T_1^{ATP} of the MC simulations is displayed over different SNRs [dB]. (B) NIIM estimates of k_{CK} over their ground-truth value and (C) the BA analyses at SNR= 12 dB.

3.2 | In vivo results

The representative in vivo MT-^{31}P-MRF signal evolutions and matching results are presented in Figure 1. The signal evolutions of PCr and γ-ATP signals were extracted from the spectra for each FA index for further matching (Figure 1D,E). As an example matching procedure, the second

iterative path with the initial condition $k_{CK}^{0,2} = 0.3\,s^{-1}$ is shown in Figure 1F–I. In each iteration step the matched dictionary entries with the measured signal evolutions are displayed. Different parts of the signal evolutions, as indicated, were used in IT1 to IT4. Note that the signal evolution of Part II is reorganised.[29]

Table 1 lists the means and STDs (six subjects) of the SNRs of PCr and γ-ATP, the pSNRs of PCr, and the estimated parameters T_1^{PCr}, T_1^{ATP}, C_r, and k_{CK} for different n_{avg}. The acquisition time includes one dummy scan. For comparison, the EBIT full-length acquisition estimates are listed. The MT-^{31}P-MRF estimates are in good agreement with those measured by EBIT. The comparison of the two methods is analysed further using the BA plot (Figure 6). Comparing the EBIT and MT-^{31}P-MRF estimates, the mean difference is below 3% for k_{CK}, 2% for T_1^{PCr}, and 12% for T_1^{ATP} with respect to the mean EBIT estimate from Table 1.

Figure 7 shows the comparison of the MT-^{31}P-MRF with EBIT over different acquisition times. For MT-^{31}P-MRF, the mean of the estimated parameter remains constant across acquisition times. The STD converges approximately for acquisition times beyond 9 min 17 s. The STD for the k_{CK} and T_1^{ATP} of EBIT doubles approximately for 5 min 30 s min acquisition time compared with the full-length acquisition. The EBIT estimate of T_1^{ATP} varies up to 70%, leading to an unsteady k_{CK} estimation with up to a 20% increase. The STDs are in general larger for EBIT compared with MT-^{31}P-MRF with the same acquisition length (except for T_1^{PCr} values at 5 min 30 s). The test–retest reproducibility is evaluated using the CV [%] of each estimated parameter. The CV for MT-^{31}P-MRF increases slightly for a reduced acquisition time of 4 min 15 s compared with the full length. The CV does not exceed 17% for k_{CK}, 19% for T_1^{PCr}, and 13% for T_1^{ATP}. Overall, the mean and STD of CV for k_{CK} and T_1^{ATP} are in the range of or lower than those of EBIT for the same acquisition time (except CV of T_1^{PCr} for 5 min 30 s).

TABLE 1 Values of estimated parameters (mean ± STD over all six subjects), SNR [dB], pSNR, and acquisition time t_{acq} for different numbers of averages (n_{avg}) compared with the EBIT results.

		MT-^{31}P-MRF						EBIT
n_{avg}		37	27	19	11	8	4	16
t_{acq}	[min:s]	17:24	12:50	9:17	5:30	4:15	2:18	17:04
SNR_{PCr}	[dB]	12.0 ± 1.1	11.3 ± 1.2	9.9 ± 1.1	8.0 ± 1.1	6.5 ± 1.1	4.3 ± 1.0	-
SNR_{ATP}	[dB]	9.8 ± 1.4	9.1 ± 1.4	7.8 ± 1.2	5.8 ± 1.2	4.6 ± 1.2	2.6 ± 0.9	-
$pSNR_{PCr}$		10.4 ± 1.6	9.9 ± 1.2	8.4 ± 1.0	6.9 ± 0.9	6.3 ± 0.8	5.0 ± 0.7	55.5 ± 10.9
k_{CK}	[s^{-1}]	0.36 ± 0.04	0.36 ± 0.04	0.38 ± 0.04	0.37 ± 0.06	0.36 ± 0.07	0.35 ± 0.08	0.37 ± 0.05
T_1^{PCr}	[s]	5.84 ± 0.37	5.87 ± 0.42	6.02 ± 0.41	5.96 ± 0.79	5.89 ± 0.97	5.78 ± 1.51	5.93 ± 0.54
T_1^{ATP}	[s]	0.86 ± 0.10	0.85 ± 0.09	0.84 ± 0.10	0.85 ± 0.14	0.86 ± 0.14	0.88 ± 0.18	0.77 ± 0.23
C_r		1.36 ± 0.12	1.36 ± 0.13	1.36 ± 0.14	1.35 ± 0.14	1.36 ± 0.16	1.36 ± 0.22	1.31 ± 0.17

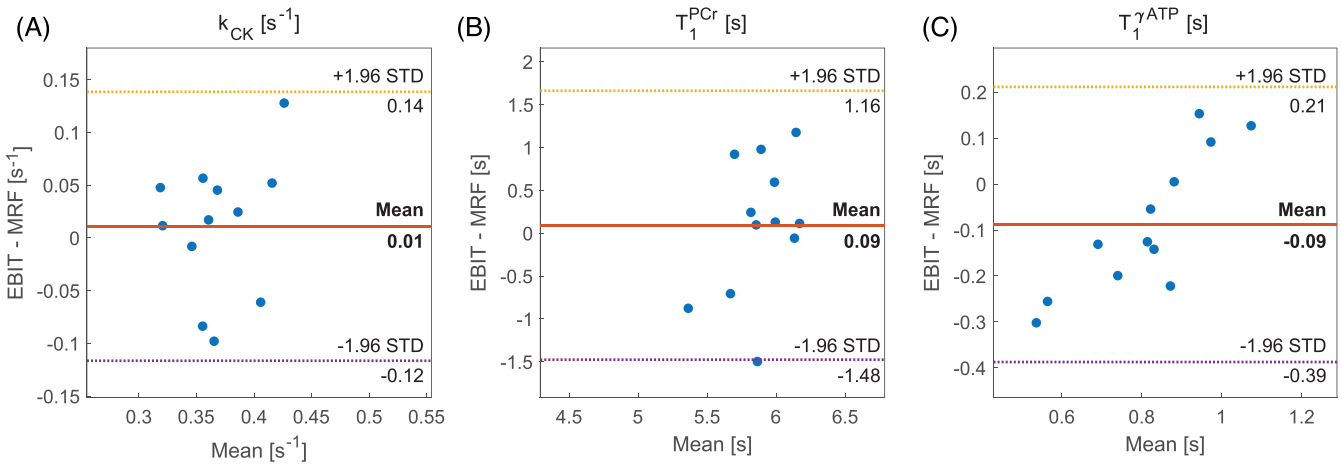

FIGURE 6 BA plots of (A) k_{CK}, (B) T_1^{PCr}, and (C) T_1^{ATP}, comparing the complete set of 12 (six subjects test–retest) in vivo estimates of EBIT and MT-^{31}P-MRF. The *x*-axis indicates means of paired estimated values by EBIT and MRF and the *y*-axis shows differences of paired measurements between EBIT and MRF. The mean differences and ±1.96 STD of the three matching parameters are illustrated in orange, yellow, and purple, respectively.

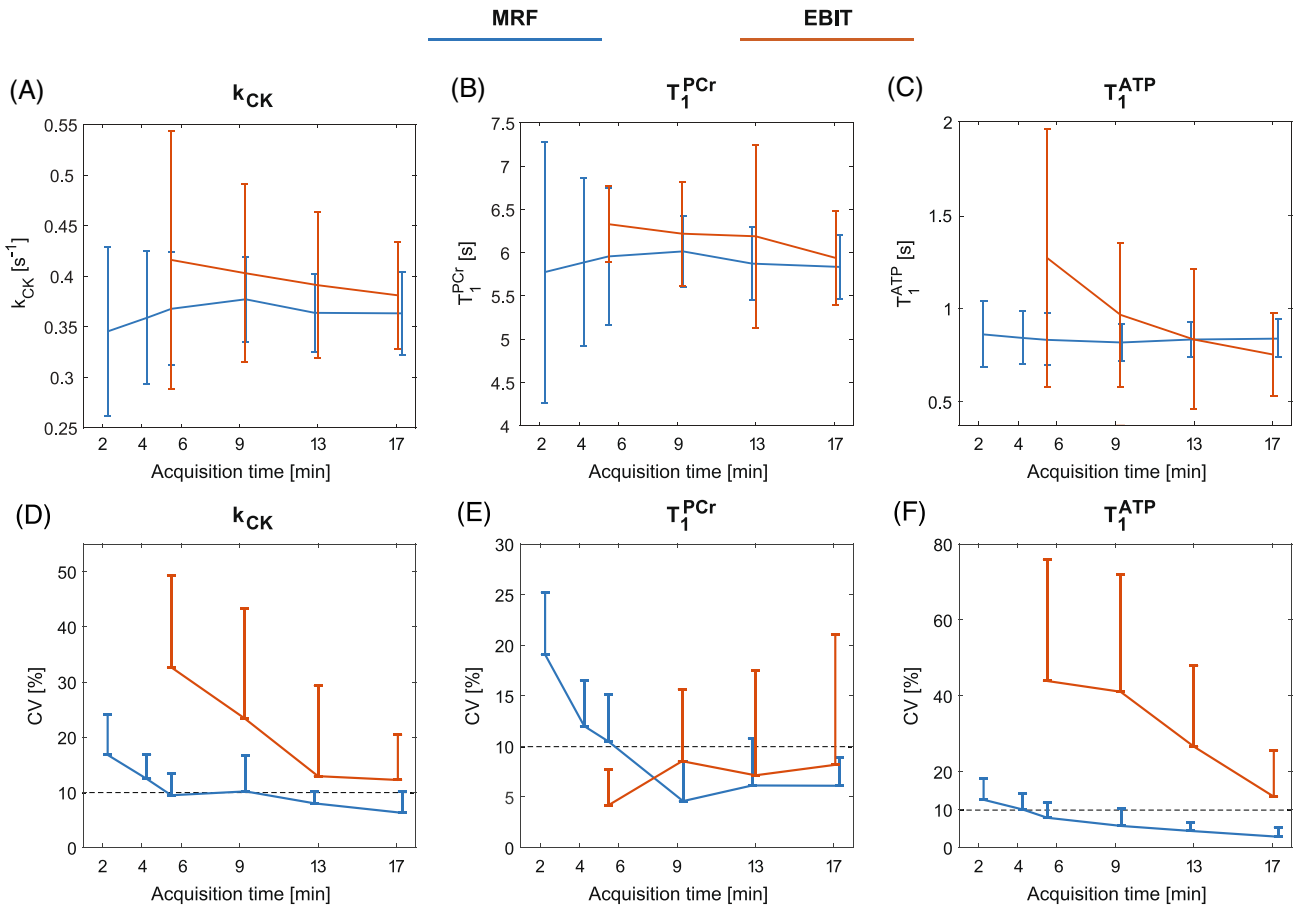

FIGURE 7 (A–C) Estimated parameters for MT-^{31}P-MRF and the EBIT method over the acquisition time. (D–F) CV [%] of MT-^{31}P-MRF and the EBIT method over the acquisition time. All values are shown as the mean and STD over all subjects and grouped averages.

4 | DISCUSSION

This study shows the feasibility of the MT-^{31}P-MRF technique for ultrafast k_{CK} in vivo assays in the human brain at 7T with a fully automated and efficient matching approach. The estimated k_{CK}, T_1^{PCr}, and T_1^{ATP} values are in excellent agreement with literature values[16,25,35] and those measured by the EBIT method.

In comparison with the estimated results of EBIT, the mean k_{CK}, T_1^{PCr}, and T_1^{ATP} values measured by MT-^{31}P-MRF do not show significant fluctuation over the scan time (Figure 7A–C), suggesting that estimation using the current approach is much less biased by noise. MT-^{31}P-MRF shows no increases in STDs up to a reduced scan time of 9 min. The increase in the STD of k_{CK}, T_1^{PCr}, and T_1^{ATP} for scan times <9 min is due to the decrease of SNR, which is in line with the results of MC simulations in Figure 5A. For the EBIT method, the STD increases significantly with the reduction in scan time. These results again indicate that MT-^{31}P-MRF together with the NIIM matching approach is a method less sensitive to low SNR, allowing ultrafast and accurate in vivo assays for k_{CK}.

k_{CK} measurement by MT-^{31}P-MRF also demonstrated superior reproducibility. The test–retest results show that, with a fourfold scan time reduction (4 min 15 s), the MT-^{31}P-MRF has a similar CV (10%) to a full-length acquisition (17 min 4) using EBIT and an improved CV over the saturation transfer method (13%).[36,37] The increase in CV of the MRF estimates for scan time <9 min (Figure 7D–F) is driven mainly by the increase in STD due to the low SNR, as discussed above. A further reduction in acquisition time at the cost of k_{CK} reproducibility (CV 17%) enables a k_{CK} measurement time within just 2 min 18 s. Moreover, T_1^{ATP} value estimation by MT-^{31}P-MRF showed substantially better reproducibility than that by EBIT; similar reproducibility performance for T_1^{PCr} estimation was achieved by both methods.

For parameter estimations in magnetic resonance fingerprinting, large dictionaries are commonly used and simulated by using the extended phase graph formalism, Bloch, or BMC equations. The number of dictionary entries is simplified and stated as m^k, where k is the number of free parameters to calculate and m is the size of incremental steps of each parameter. With increasing number of parameters, the computational load and required memory size increase exponentially. Therefore, classical dictionary simulation is becoming unrealistic for high-order parameter

estimation even for supercomputers and especially in clinical setups. In this study, the problem set led to a total of six parameters to estimate. In comparison with the previous study in rodent limbs,[27] C_{B1} and T_1^{ATP} have additionally been incorporated. To the best of our knowledge, this is so far the largest parameter set being estimated in the MRF framework. To address the challenge of creating and matching large multiparametric dictionaries, we introduce NIIM. NIIM combines an efficient low-dimensional iterative parameter estimation with an interpolation approach to converge towards a bias-free estimation in 1 min 30 s post-processing time with 55 MB of data per subject. In the iteration part, each of the five loops is an independent parameter estimation process based on varying initial conditions $k_{CK}^{0,n}$. Each iterative step inside a loop estimates two (IT1) or one (IT2 to IT4) parameter(s) using a dictionary with two or one parameters varied and the other four or five parameters fixed, respectively. As such, the interdependence of the parameters on fingerprint matching is not accounted for in these iterative steps. Therefore, the estimates are biased depending on the initial condition of $k_{CK}^{0,n}$. The relationship between the introduced bias in the estimates and the initial condition $k_{CK}^{0,n}$ was approximated using a linear regression in the problem examined. This relation was validated by simulations (Figures 4 and 5) and used in the interpolation part for the bias correction. As this is a proof-of-concept application of NIIM, it is important to note that the linear approximation may not be generally valid. Outside the examined parameter range, a linear approximation might not be sufficient and nonlinear regression functions, for example, higher order polynomials, might be needed and should be investigated in future work. Further, the NIIM can be extended for applications in other organs such as skeletal muscles,[38,39] liver,[40] and heart.[41,42] To do so, the initial condition and values might need to be adjusted to the expected value range for the respective organ. Moreover, NIIM could be extended to other multiparametric MRF problems, such as chemical exchange dependent saturation transfer.[43,44] Note that, in all extended use cases, estimation order and the regression function need to be re-evaluated and possibly adapted.

The FA pattern used for MT-^{31}P-MRF follows a sinusoidal shape in Parts I and III.[28,45] The number of FAs of the sinusoidal after the inversion pulses is set according to the T_1 relaxation rates of PCr (after GI1 and 2; AI1) and γ-ATP (AI2) in the human brain to display the recovery process. We incorporated two GIs in Part I to increase the sensitivity for T_1 estimation (supplementary material S4, Table S4.1) and the two AIs in Part III to increase the sensitivity for k_{CK}.[46,47] Together with the fast-changing part (Part III),[29] the pattern features a good noise robustness and estimation accuracy, as shown in the MC simulations. Note that the FA pattern presented is a proof of concept and further optimisation techniques can be applied to improve the pattern.[48–53]

Surface coils are commonly used and are advantageous in ^{31}P MRS studies due to their high signal sensitivity. However, the major drawback is their strong transmit field inhomogeneity. Unlike the original MRF method,[28] neither a homogeneous B_1 field nor an ideal FA can be assumed in the excited volume. As stated in previous publications,[28,29,31] accurate B_1 knowledge plays a key role in bias-free estimations. Measuring the B_1 field map in the ^{31}P human brain results in long scan times; thus, in the current study, this is not applicable. Therefore, the B_1 estimation was included in the matching procedure. To proceed matching on Part II of the pattern,[29] a linear coil sensitivity approximation and slice profile correction are issued. In future studies, matching errors introduced by B_1 field inhomogeneity can be addressed by using a volume coil with improved transmit field homogeneity or the incorporation of B_1 field prior knowledge, as suggested previously.[31]

At ultrahigh field (7T), the existence of B_0 inhomogeneities is a known complication. The bSSFP-like architecture of MT-^{31}P-MRF, as stated in the original MRF approach,[28] shows strong variations in the signal evolution induced by those field changes. The size of the excited volume made it necessary to incorporate more than one isochromat to represent the different off-resonance frequencies in the excited volume. The distribution of the field (and thus isochromats) is found by measuring a B_0 field map over the excited slice. Furthermore, the frequency between PCr and γ-ATP was fixed to -2.52 ppm in this study, since only healthy volunteers were observed. However, the resonance frequency of γ-ATP can change due to magnesium concentrations.[54,55] This issue can be addressed either by including the off-resonance of γ-ATP separately in the estimation process or by using pilot scans.

Similar to the study of Wang et al.,[27] T_2 values of PCr and γ-ATP are fixed according to the literature[32] to reduce the complexity of the parameter estimation. Since T_2 parameters are not estimated in the current matching approach, an incorrect assumption in T_2 values may lead to a bias in parameter estimations, especially for k_{CK}. To date, no studies have reported pathological or physiologically induced changes in the T_2 values of PCr and γ-ATP in the human brain. However, changes in the T_2 relaxation times of ^{1}H metabolites have been reported during brain development and in ischaemic tissues.[56,57] In another ^{1}H MRS study, significant T_2 changes (45%) of N-acetyl aspartate were observed in glioma patients.[58] To avoid potential ME in the model due to pathologically or physiologically induced changes in T_2, the current matching approach needs to be developed further with the incorporation of T_2 estimation.

In conclusion, we showed that MT-^{31}P-MRF combined with NIIM is a new and robust tool in the MRF framework to study human brain metabolism. The newly introduced NIIM presents an efficient tool for MRF studies with high-dimensional problem sets. With MT-^{31}P-MRF, faster and more reproducible measurements are possible compared with the state-of-the-art method, which enables the potential to investigate brain energy metabolism in a clinical setting.

AUTHOR CONTRIBUTIONS

MW and SL: conceptualization, methodology, experiments, data processing, writing original draft and review. DW: hardware support and review of draft. LX: conceptualization, methodology, writing original draft and review, supervision, resources, data curation, funding acquisition.

ACKNOWLEDGEMENTS

We thank K. Pierzchala for helping us in preparing solutions for the phantoms.

This work was supported by the Swiss National Science Foundation (grant no. 320030_189064). We acknowledge access to the facilities and expertise of the CIBM Center for Biomedical Imaging, a Swiss research center of excellence founded and supported by Lausanne University Hospital (CHUV), University of Lausanne (UNIL), Ecole polytechnique fédérale de Lausanne (EPFL), University of Geneva (UNIGE), and Geneva University Hospitals (HUG). Open access funding provided by Ecole Polytechnique Federale de Lausanne.

CONFLICT OF INTEREST STATEMENT

None of the authors declares a conflict of interest.

REFERENCES

1. Wallimann T, Dolder M, Schlattner U, et al. Creatine kinase: An enzyme with a central role in cellular energy metabolism. *Magnet Reson Mater Phys Biol Med*. 1998;6(2):116-119. https://www.sciencedirect.com/science/article/pii/S1352866198000349
2. Chen W, Zhu X-H, Adriany G, Ugˇurbil K. Increase of creatine kinase activity in the visual cortex of human brain during visual stimulation: A 31P NMR magnetization transfer study. *Magnet Reson Med*. 1997;38(4):551-557. https://onlinelibrary.wiley.com/doi/abs/10.1002/mrm.1910380408
3. Smith CD, Landrum W, Carney JM, Landfield PW, Avison MJ. Brain creatine kinase with aging in F-344 rats: Analysis by saturation transfer magnetic resonance spectroscopy. *Neurobiol Aging*. 1997;18(6):617-622.
4. Du F, Yuksel C, Chouinard V-A, et al. Abnormalities in high-energy phosphate metabolism in first-episode bipolar disorder measured using 31P-magnetic resonance spectroscopy. *Biolog Psychiat*. 2018;84(11):797-802. https://www.sciencedirect.com/science/article/pii/S000632231731466X
5. Yuksel C, Chen X, Chouinard V-A, et al. Abnormal brain bioenergetics in first-episode psychosis. *Schizophrenia Bull Open*. 2021;2(1):sgaa073. doi:10.1093/schizbullopen/sgaa073
6. Du F, Cooper AJ, Thida T, et al. In vivo evidence for cerebral bioenergetic abnormalities in schizophrenia measured using 31P magnetization transfer spectroscopy. *JAMA Psychiat*. 2014;71(1):19-27. doi:10.1001/jamapsychiatry.2013.2287
7. Shoubridge EA, Briggs RW, Radda GK. 31P NMR saturation transfer measurements of the steady state rates of creatine kinase and ATP synthetase in the rat brain. *FEBS Lett*. 1982;140(2):288-292. https://www.sciencedirect.com/science/article/pii/0014579382809162
8. Du F, Zhu X-H, Qiao H, Zhang X, Chen W. Efficient in vivo 31P magnetization transfer approach for noninvasively determining multiple kinetic parameters and metabolic fluxes of ATP metabolism in the human brain. *Magnet Reson Med*. 2007;57(1):103-114. https://onlinelibrary.wiley.com/doi/abs/10.1002/mrm.21107
9. Bottomley PA, Ouwerkerk R, Lee RF, Weiss RG. Four-angle saturation transfer (FAST) method for measuring creatine kinase reaction rates in vivo. *Magnet Reson Med*. 2002;47(5):850-863. https://onlinelibrary.wiley.com/doi/abs/10.1002/mrm.10130
10. Schär M, El-Sharkawy A-MM, Weiss RG, Bottomley PA. Triple repetition time saturation transfer (TRiST) 31P spectroscopy for measuring human creatine kinase reaction kinetics. *Magnet Reson Med*. 2010;63(6):1493-1501. https://onlinelibrary.wiley.com/doi/abs/10.1002/mrm.22347
11. Schär M, Gabr RE, El-Sharkawy A-MM, Steinberg A, Bottomley PA, Weiss RG. Two repetition time saturation transfer (TwiST) with spill-over correction to measure creatine kinase reaction rates in human hearts. *J Cardiovasc Magnet Reson*. 2015;17(1):70. doi:10.1186/s12968-015-0175-4
12. Xiong Q, Du F, Zhu X, et al. ATP production rate via creatine kinase or ATP synthase in vivo. *Circul Res*. 2011;108(6):653-663. https://www.ahajournals.org/doi/full/10.1161/CIRCRESAHA.110.231456, Publisher: American Heart Association.
13. Balaban RS, Koretsky AP. Interpretation of 31P NMR saturation transfer experiments: What you can't see might confuse you. Focus on "Standard magnetic resonance-based measurements of the Pi→ ATP rate do not index the rate of oxidative phosphorylation in cardiac and skeletal muscles". *Am J Physiol-Cell Physiol*. 2011;301(1):C12-C15. https://journals.physiology.org/doi/full/10.1152/ajpcell.00100.2011. Publisher: American Physiological Society.
14. Spencer RGS, Fishbein KW, Galban CJ. Pitfalls in the measurement of metabolite concentrations using the one-pulse experiment in in vivo NMR: Commentary on "On neglecting chemical exchange effects when correcting in Vivo31P MRS data for partial saturation" (2001;149(2):251–257). *J Magnet Reson*. 2001;151(2):347-348. https://www.sciencedirect.com/science/article/pii/S1090780701923985
15. Gabr RE, Weiss RG, Bottomley PA. Correcting reaction rates measured by saturation-transfer magnetic resonance spectroscopy. *J Magnet Reson*. 2008;191(2):248-258. https://www.sciencedirect.com/science/article/pii/S1090780707003837
16. Ren J, Sherry AD, Malloy CR. Efficient 31P band inversion transfer approach for measuring creatine kinase activity, ATP synthesis, and molecular dynamics in the human brain at 7 T. *Magnet Reson Med*. 2017;78(5):1657-1666. https://onlinelibrary.wiley.com/doi/abs/10.1002/mrm.26560
17. Degani H, Alger JR, Shulman RG, Petroff OAC, Prichard JW. 31P magnetization transfer studies of creatine kinase kinetics in living rabbit brain. *Magnet Reson Med*. 1987;5(1):1-12. https://onlinelibrary.wiley.com/doi/abs/10.1002/mrm.1910050102
18. Mora BN, Narasimhan PT, Ross BD. 31P magnetization transfer studies in the monkey brain. *Magnet Reson Med*. 1992;26(1):100-115 en. https://onlinelibrary.wiley.com/doi/abs/10.1002/mrm.1910260111
19. Buehler T, Kreis R, Boesch C. Comparison of 31P saturation and inversion magnetization transfer in human liver and skeletal muscle using a clinical MR system and surface coils. *NMR Biomed*. 2015;28(2):188-199. https://onlinelibrary.wiley.com/doi/abs/10.1002/nbm.3242
20. Joubert F, Gillet B, Mazet JL, Mateo P, Beloeil JC, Hoerter JA. Evidence for myocardial ATP compartmentation from NMR inversion transfer analysis of creatine kinase fluxes. *Biophys J*. 2000;79(1):1-13. https://www.sciencedirect.com/science/article/pii/S0006349500762692
21. Bogner W, Chmelik M, Schmid A, Moser E, Trattnig S, Gruber S. Assessment of 31P relaxation times in the human calf muscle: A comparison between 3 T and 7 T in vivo. *Magnet Reson Med*. 2009;62(3):574-582. https://onlinelibrary.wiley.com/doi/abs/10.1002/mrm.22057
22. Boeck CR, Carbonera LS, Milioli ME, et al. Mitochondrial respiratory chain and creatine kinase activities following trauma brain injury in brain of mice preconditioned with N-methyl-d-aspartate. *Molecul Cellular Biochem*. 2013;384(1):129-137. doi:10.1007/s11010-013-1790-8
23. Hsieh PS, Balaban RS. Saturation and inversion transfer studies of creatine kinase kinetics in rabbit skeletal muscle in vivo. *Magnet Reson Med*. 1988;7(1):56-64. https://onlinelibrary.wiley.com/doi/abs/10.1002/mrm.1910070107

24. Pouymayou B, Buehler T, Kreis R, Boesch C. Test–retest analysis of multiple 31P magnetization exchange pathways using asymmetric adiabatic inversion. *Magnet Reson Med*. 2017;78(1):33-39. https://onlinelibrary.wiley.com/doi/abs/10.1002/mrm.26337
25. Ren J, Yang B, Sherry AD, Malloy CR. Exchange kinetics by inversion transfer: Integrated analysis of the phosphorus metabolite kinetic exchanges in resting human skeletal muscle at 7 T. *Magnet Reson Med*. 2015;73(4):1359-1369. https://onlinelibrary.wiley.com/doi/abs/10.1002/mrm.25256
26. Ren J, Sherry AD, Malloy CR. Modular 31P wideband inversion transfer for integrative analysis of adenosine triphosphate metabolism, T1 relaxation and molecular dynamics in skeletal muscle at 7T. *Magnet Reson Med*. 2019;81(6):3440-3452. https://onlinelibrary.wiley.com/doi/abs/10.1002/mrm.27686
27. Wang CY, Liu Y, Huang S, Griswold MA, Seiberlich N, Yu X. 31P magnetic resonance fingerprinting for rapid quantification of creatine kinase reaction rate in vivo. *NMR Biomed*. 2017;30(12):e3786. https://onlinelibrary.wiley.com/doi/abs/10.1002/nbm.3786
28. Ma D, Gulani V, Seiberlich N, et al. Magnetic resonance fingerprinting. *Nature*. 2013;495(7440):187-192. https://www.nature.com/articles/nature11971. Publisher: Nature Publishing Group.
29. Buonincontri G, Schulte RF, Cosottini M, Tosetti M. Spiral MR fingerprinting at 7T with simultaneous B1 estimation. *Magnet Reson Imaging*. 2017;41:1-6. https://www.sciencedirect.com/science/article/pii/S0730725X17300747
30. Hwang T-L, van Zijl PCM, Garwood M. Asymmetric adiabatic pulses for NH selection. *J Magnet Reson*. 1999;138(1):173-177. https://www.sciencedirect.com/science/article/pii/S1090780799917135
31. Ma D, Coppo S, Chen Y, et al. Slice profile and B1 corrections in 2D magnetic resonance fingerprinting. *Magnet Reson Med*. 2017;78(5):1781-1789. https://onlinelibrary.wiley.com/doi/abs/10.1002/mrm.26580
32. Lei H, Zhu X-H, Zhang X-L, Ugurbil K, Chen W. In vivo 31P magnetic resonance spectroscopy of human brain at 7 T: An initial experience. *Magnet Reson Med*. 2003;49(2):199-205. https://onlinelibrary.wiley.com/doi/abs/10.1002/mrm.10379
33. Mispelter J, Lupu M, Briguet A. *NMR Probeheads For Biophysical And Biomedical Experiments: Theoretical Principles And Practical Guidelines*. 2nd ed.: World Scientific Publishing Company; 2015. Google-Books-ID: Iec7DQAAQBAJ.
34. Myles PS, Cui JI. Using the Bland–Altman method to measure agreement with repeated measures. *BJA: British J Anaesthesia*. 2007;99(3):309-311. doi:10.1093/bja/aem214
35. Valkovič L, Chmelík M, Just Kukurova I, et al. Time-resolved phosphorous magnetization transfer of the human calf muscle at 3T and 7T: A feasibility study. *Eur J Radiol*. 2013;82(5):745-751. https://www.sciencedirect.com/science/article/pii/S0720048X11007790
36. Xin L, Ipek, Beaumont M, et al. Nutritional ketosis increases NAD+/NADH ratio in healthy human brain: An in vivo study by 31P-MRS. *Front Nutrition*. 2018;5:62. https://www.frontiersin.org/article/10.3389/fnut.2018.00062
37. Xin L, Ipek Ö, Cuenoud B, Beaumont M, Shevlyakova M, Gruetter R. Reproducibility of of metabolism measured by 31P MRS in human brain: A test–retest study at 7T. ESMRMB 2017, Abstract 943.
38. Shoubridge EA, Bland JL, Radda GK. Regulation of creatine kinase during steady-state isometric twitch contraction in rat skeletal muscle. *Biochim et Biophys Acta (BBA)-Molec Cell Res*. 1984;805(1):72-78.
39. Kushmerick MJ. Energy balance in muscle activity: simulations of ATPase coupled to oxidative phosphorylation and to creatine kinase. *Comparat Biochem Physiol Part B: Biochem Molec Biol*. 1998;120(1):109-123.
40. Li Z, Qiao H, Lebherz C, et al. Creatine kinase, a magnetic resonance-detectable marker gene for quantification of liver-directed gene transfer. *Human Gene Therapy*. 2005;16(12):1429-1438. https://www.liebertpub.com/doi/abs/10.1089/hum.2005.16.1429
41. Bottomley PA, Panjrath GS, Lai S, et al. Metabolic rates of ATP transfer through creatine kinase (CK flux) predict clinical heart failure events anddeath. *Sci Transl Med*. 2013;5(215):215re3. https://www.science.org/doi/full/10.1126/scitranslmed.3007328
42. Weiss RG, Gerstenblith G, Bottomley PA. ATP flux through creatine kinase in the normal, stressed, and failing human heart. *Proc Nat Acad Sci*. 2005;102(3):808-813. https://www.pnas.org/doi/abs/10.1073/pnas.0408962102
43. Ward KM, Aletras AH, Balaban RS. A new class of contrast agents for MRI based on proton chemical exchange dependent saturation transfer (CEST). *J Magnet Reson*. 2000;143(1):79-87. https://www.sciencedirect.com/science/article/pii/S1090780799919560
44. Cohen O, Huang S, McMahon MT, Rosen MS, Farrar CT. Rapid and quantitative chemical exchange saturation transfer (CEST) imaging with magnetic resonance fingerprinting (MRF). *Magnet Reson Med*. 2018;80(6):2449-2463. https://onlinelibrary.wiley.com/doi/abs/10.1002/mrm.27221
45. Jiang Y, Ma D, Seiberlich N, Gulani V, Griswold MA. MR fingerprinting using fast imaging with steady state precession (FISP) with spiral readout. *Magnet Reson Med*. 2015;74(6):1621-1631. https://onlinelibrary.wiley.com/doi/abs/10.1002/mrm.25559
46. Ren J, Sherry AD, Malloy CR. 31P-MRS of healthy human brain: ATP synthesis, metabolite concentrations, pH, and T1 relaxation times. *NMR Biomed*. 2015;28(11):1455-1462. https://onlinelibrary.wiley.com/doi/abs/10.1002/nbm.3384
47. Ren J, Sherry AD, Malloy CR. Amplification of the effects of magnetization exchange by 31P band inversion for measuring adenosine triphosphate synthesis rates in human skeletal muscle. *Magnet Reson Med*. 2015;74(6):1505-1514. https://onlinelibrary.wiley.com/doi/abs/10.1002/mrm.25514
48. Sommer K, Amthor T, Doneva M, Koken P, Meineke J, Börnert P. Towards predicting the encoding capability of MR fingerprinting sequences. *Magnet Reson Imaging*. 2017;41:7-14. https://www.sciencedirect.com/science/article/pii/S0730725X17301182
49. Heesterbeek DGJ, Koolstra K, van Osch MJP, van Gijzen MB, Vos FM, Nagtegaal MA. Mitigating undersampling errors in MR fingerprinting by sequence optimization. *Magnet Reson Med*. 2023;89(5):2076-2087. https://onlinelibrary.wiley.com/doi/abs/10.1002/mrm.29554
50. Cohen O, Rosen MS. Algorithm comparison for schedule optimization in MR fingerprinting. *Magnet Reson Imag*. 2017;41:15-21. https://www.sciencedirect.com/science/article/pii/S0730725X17300437
51. Wong ML, Wu EZC, Wong EC. (ISMRM 2014) Optimization of Flip angle and TR schedules for MR Fingerprinting. ISMRM 2014; Abstract 1469. https://archive.ismrm.org/2014/1469.html
52. Hamilton JI, Wright KL, Jiang Y, et al. (ISMRM 20) Pulse Sequence Optimization for Improved MRF Scan Efficiency. ISMRM 2015; Abstract 3386. https://archive.ismrm.org/2015/3386.html
53. Lin, T-M, Chiu, S-C, Cheng, C-C, Wu, W-C, Chung, H-W. Quantitative evaluation of the effect of reduction of signal acquisition number in MR fingerprinting. ISMRM 2015; Abstract 3388. https://archive.ismrm.org/2015/3388.html

54. Iotti S, Frassineti C, Alderighi L, Sabatini A, Vacca A, Barbiroli B. In vivo assessment of free magnesium concentration in human brain by 31P MRS. A new calibration curve based on a mathematical algorithm. *NMR Biomed*. 1996;9(1):24-32. https://onlinelibrary.wiley.com/doi/abs/10.1002/%28SICI%291099-1492%281%99602%299%3A1%3C24%3A%3AAID-NBM392%3E3.0.CO%3B2-B
55. Iotti S, Frassineti C, Alderighi L, Sabatini A, Vacca A, Barbiroli B. In vivo 31P-MRS assessment of cytosolic [Mg2+] in the human skeletal muscle in different metabolic conditions. *Magnet Reson Imaging*. 2000;18(5):607-614. https://www.sciencedirect.com/science/article/pii/S0730725X00001326
56. Larvaron P, Bielicki G, Boespflug-Tanguy O, Renou J-P. Proton MRS of early post-natal mouse brain modifications in vivo. *NMR Biomed*. 2006;19(2):180-187. https://onlinelibrary.wiley.com/doi/abs/10.1002/nbm.997
57. Lei H, Zhang Y, Zhu X-H, Chen W. Changes in the proton T2 relaxation times of cerebral water and metabolites during forebrain ischemia in rat at 9.4 T. *Magnet Reson Med*. 2003;49(6):979-984. https://onlinelibrary.wiley.com/doi/abs/10.1002/mrm.10490
58. Isobe T, Matsumura A, Anno I, et al. Quantification of cerebral metabolites in glioma patients with proton MR spectroscopy using T2 relaxation time correction. *Magnet Reson Imag*. 2002;20(4):343-349. https://www.sciencedirect.com/science/article/pii/S0730725X02005003

SUPPORTING INFORMATION

Additional supporting information can be found online in the Supporting Information section at the end of this article.

How to cite this article: Widmaier M, Lim S-I, Wenz D, Xin L. Fast in vivo assay of creatine kinase activity in the human brain by ^{31}P magnetic resonance fingerprinting. *NMR in Biomedicine*. 2023;e4998. doi:10.1002/nbm.4998